Study on the Flow Characteristics and Heating Performance of a Drilling Fluid Helical Heater

Yi Zhang[1,*], Daqin Zhang[1], Zhen Wang[1] and Bangyao Tang[1]

[1] School of Mechatronic Engineering, Southwest Petroleum University. Chengdu 610500, China
* Correspondence: dream5568@126.com

Abstract: Gas logging technology plays a critical role in petroleum drilling. Within this system, the degasser serves as a key component, and the heater is an essential part of the degassing unit. Heating the drilling fluid promotes more efficient liberation of hydrocarbon gases, thereby enhancing the accuracy of gas logging. Therefore, improving the heater's heat transfer performance is of significant importance for optimizing logging operations. In this study, numerical simulation is employed to investigate the heating and flow characteristics of return drilling fluid inside the channels of a spiral heater. The effects of the heater's structural parameters and the operational conditions of the drilling fluid on its heating performance are systematically analyzed. Furthermore, experimental studies on the spiral heater were conducted, and the differences between numerical simulations and experimental results were evaluated for two different helix pitches under varying flow rates.

Keywords: drilling fluid, heater, spiral fin, heat transfer

1. Introduction

As the depth and complexity of oil and gas exploration continue to increase, the analysis and identification of drilling fluid returning from the annulus have become crucial for discovering hydrocarbon zones and evaluating reservoirs [1]. The degasser is a key separation device widely used in gas logging systems during petroleum drilling. A three-dimensional schematic of the designed degasser is presented in Figure 1.

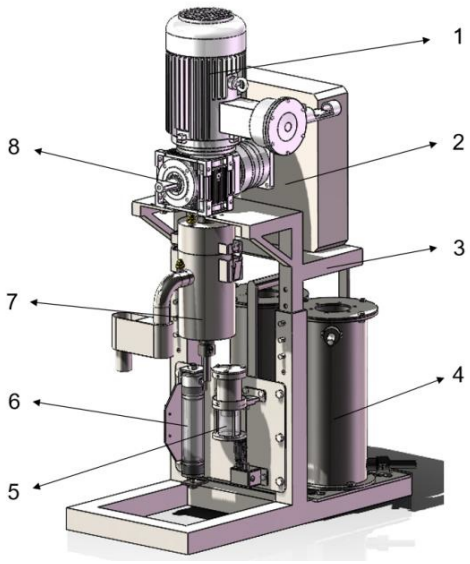

Figure 1. Three-dimensional design of degasser. (1-motor 2-pump 3-stand 4-heater 5-dehumidifier 6-condenser 7-degassing chamber 8-reducer)

Citation: Yi Zhang, Daqin Zhang, Zhen Wang and Bangyao Tang. 2025. Study on the Flow Characteristics and Heating Performance of a Drilling Fluid Helical Heater. *TK Techforum Journal (ThyssenKrupp Techforum)* 2025(1): 41–55.
https://doi.org/10.71448/tk202544

Received: 30-October-2025
Revised: 01-November-2025
Accepted: 25-November-2025
Published: 02-December-2025

Heating the drilling fluid prior to agitation and degassing promotes more efficient liberation of entrained hydrocarbon gases. However, under field conditions—especially in unconsolidated formations—the heater's performance is highly dependent on the properties of the drilling fluid [2]. Therefore, it is essential to investigate how the heater's structural parameters and the operational conditions of the drilling fluid influence its thermal performance.

In recent years, numerous theoretical and experimental studies have been conducted to enhance heat transfer efficiency and reduce energy consumption in heat exchangers. For instance, Wang et al. [3] developed a novel multi-coiled tube heat exchanger to overcome the large footprint of conventional straight-tube designs and used numerical simulations to analyze the effects of structural and flow parameters on heat transfer and flow resistance. Zhang et al. [4] experimentally studied the thermal and flow resistance characteristics of integral spiral finned tube (IRSFT) bundles, observing that the Nusselt number (Nu) increases with both transverse and longitudinal pitch, while it first increases and then decreases with fin pitch and fin height. Ali et al. [5] evaluated the thermal performance of a shell-and-spiral-tube heat exchanger, considering parameters such as displacement, velocity coefficient, and friction coefficient. Esfe et al. [6] combined numerical and experimental methods to examine the influence of a coiled-tube turbulator on heat transfer and pressure drop in a counter-flow shell-and-tube heat exchanger, comparing the results with a straight spiral coil design.

Additionally, various optimization and prediction algorithms have been integrated into heat exchanger performance studies [7]. Zhang et al. [8] applied a multi-objective genetic algorithm (NSGA-II) to optimize a neural network model for predicting heat transfer coefficients and pressure drops in tube-fin heat exchangers, presenting optimal results in the form of a Pareto front. Petrovic et al. [9] used topology optimization to design fins for plate-fin heat exchangers, leading to notable performance improvements.

However, there remains limited research focusing specifically on the flow and heating behavior of return drilling fluid inside spiral heaters. Although numerous studies have explored heat transfer enhancement using spiral coils [10–14]—for example, Keklikcioglu et al. [15] experimentally demonstrated enhanced heat transfer in tubes fitted with triangular spiral inserts, albeit with increased friction losses; Promvonge [16] compared thermal and flow characteristics of tubes enhanced with square and circular spiral coils; Zohir et al. [17] reported that circular spiral coils significantly improve heat transfer in double-pipe heat exchangers; Ibrahim et al. [18] showed that spiral-finned flat tubes outperform circular ones; and Ard et al. [19] experimentally studied concentric double-pipe heat exchangers with spiral fins, both with and without cores—studies that address the specific application to drilling fluid in spiral heaters are scarce.

Despite extensive theoretical and experimental research on drilling fluid heating systems by various scholars and industry experts, there is still a notable lack of studies examining how drilling fluid heating affects degassing efficiency, particularly regarding the combined influence of fluid properties and spiral heater geometry on thermal performance. To address this gap, this study designs a spiral heater and adopts an integrated numerical and experimental approach to analyze the effects of key drilling fluid parameters and heater structural configurations on heating performance, with the goal of improving the overall thermal efficiency of the heater.

2. Theoretical method and heater heat-transfer model

2.1. Governing equations

Computational fluid dynamics (CFD) primarily uses computer-based numerical methods to solve the governing equations of fluid mechanics and to simulate and analyze fluid flow problems. In the coupling process, the continuous phase must satisfy the mass conservation equation, the momentum equations, and the energy conservation equation. The fluid is assumed to be incompressible, and heat exchange between the heater and the

drilling fluid is considered. Based on these assumptions, the governing equations for heat transfer and fluid motion are derived.

Continuity equation:

$$\frac{\partial u}{\partial x} + \frac{\partial v}{\partial y} + \frac{\partial w}{\partial z} = 0, \tag{1}$$

where u, v, and w are the velocity components in the x, y, and z directions, respectively.

Momentum equations:

$$u\frac{\partial u}{\partial x} + v\frac{\partial u}{\partial y} + w\frac{\partial u}{\partial z} = -\frac{1}{\rho_w}\frac{\partial p}{\partial x} + \frac{\mu_w}{\rho_w}\left(\frac{\partial^2 u}{\partial x^2} + \frac{\partial^2 u}{\partial y^2} + \frac{\partial^2 u}{\partial z^2}\right), \tag{2}$$

$$u\frac{\partial v}{\partial x} + v\frac{\partial v}{\partial y} + w\frac{\partial v}{\partial z} = -\frac{1}{\rho_w}\frac{\partial p}{\partial y} + \frac{\mu_w}{\rho_w}\left(\frac{\partial^2 v}{\partial x^2} + \frac{\partial^2 v}{\partial y^2} + \frac{\partial^2 v}{\partial z^2}\right), \tag{3}$$

$$u\frac{\partial w}{\partial x} + v\frac{\partial w}{\partial y} + w\frac{\partial w}{\partial z} = -\frac{1}{\rho_w}\frac{\partial p}{\partial z} + \frac{\mu_w}{\rho_w}\left(\frac{\partial^2 w}{\partial x^2} + \frac{\partial^2 w}{\partial y^2} + \frac{\partial^2 w}{\partial z^2}\right), \tag{4}$$

where ρ_w and μ_w denote the density and dynamic viscosity of water, respectively.

The energy equation is written as

$$\frac{k_w}{\rho_w C_{pw}}\left(\frac{\partial^2 T_w}{\partial x^2} + \frac{\partial^2 T_w}{\partial y^2} + \frac{\partial^2 T_w}{\partial z^2}\right) = u\frac{\partial T_w}{\partial x} + v\frac{\partial T_w}{\partial y} + w\frac{\partial T_w}{\partial z}, \tag{5}$$

where T_w is the water temperature, C_{pw} is the specific heat, and k_w is the thermal conductivity of water.

Turbulence models in CFD mainly include the Spalart–Allmaras model, Reynolds-averaged Navier–Stokes (RANS) models, and large eddy simulation (LES) models. The k–ε model is the most widely used in practical engineering flow calculations [20]. The drilling fluid has high viscosity, and the turbulence varies significantly in the spiral heater flow. The standard k–ε model proposed by Launder and Spalding has stable performance and high calculation accuracy. Therefore, the standard k–ε model is selected as the turbulence model for the numerical simulation.

The transport equations for the turbulent kinetic energy k and its dissipation rate ε are given in (6)–(7):

$$\frac{\partial(\rho_w k)}{\partial t} + \frac{\partial(\rho_w k u_i)}{\partial x_j} = \frac{\partial}{\partial x_j}\left[\left(\mu_l + \frac{\mu_t}{\sigma_k}\right)\frac{\partial k}{\partial x_j}\right] + G_k + G_b - \rho_w\varepsilon - Y_m + S_k, \tag{6}$$

$$\frac{\partial(\rho_w \varepsilon)}{\partial t} + \frac{\partial(\rho_w \varepsilon u_i)}{\partial x_j} = \frac{\partial}{\partial x_j}\left[\left(\mu_l + \frac{\mu_t}{\sigma_\varepsilon}\right)\frac{\partial \varepsilon}{\partial x_j}\right] + C_{1\varepsilon}\frac{\varepsilon}{k}\left(G_k + C_{2\varepsilon}\rho_w\frac{\varepsilon^2}{k}\right) + S_\varepsilon, \tag{7}$$

where k is the turbulent kinetic energy; ε is the dissipation rate of turbulent kinetic energy; μ_i is the mean velocity; x_j is the spatial coordinate; μ_l is the laminar viscosity coefficient; μ_t is the turbulent viscosity coefficient; G_k is the turbulent kinetic energy generated by the mean velocity gradients; G_b is the turbulent kinetic energy generated by buoyancy; Y_m represents the contribution of the fluctuating dilatation in compressible turbulence to the overall dissipation rate; $C_{1\varepsilon}$, $C_{2\varepsilon}$, σ_k, and σ_ε are empirical constants; and S_k and S_ε are source terms.

The reverse drilling fluid can be considered an incompressible fluid, so

$$G_b = 0, \quad Y_m = 0, \quad S_k = 0, \quad S_\varepsilon = 0, \quad C_{1\varepsilon} = 1.44, \quad C_{2\varepsilon} = 1.92, \quad \sigma_\varepsilon = 1.3, \quad \sigma_k = 1.0.$$

2.2. Heat transfer performance evaluation index

In this paper, the main heat transfer mode of the spiral heater is convective heat transfer. When the fluid contacts the surface of the spiral fin, there is relative motion between the fluid and the fin wall, and, due to the temperature difference between them,

heat is transferred. The Nusselt number Nu characterizes the intensity of convective heat transfer in the analysis of the fluid flow. In the heat transfer problem of a heat exchanger, the larger the Nusselt number, the more significant the convective heat transfer effect inside the heater. The expression for the Nusselt number is shown in Eq. (8):

$$\mathrm{Nu} = \frac{h_0 D_e}{\lambda_0}. \tag{8}$$

In this equation, h_0 is the average convective heat transfer coefficient and λ_0 is the thermal conductivity. For complex shapes, the characteristic length can be defined as in Eq. (9):

$$D_e = \frac{V_f}{A_f}, \tag{9}$$

where V_f denotes the volume of the fluid and A_f represents the surface area of the fluid.

The formulae for calculating the average convective heat transfer coefficient h_0 are shown in Eqs. (10)–(13):

$$h_0 = \frac{Q}{A_0(\overline{T}_{\mathrm{wall}} - T_\infty)}, \tag{10}$$

$$Q = \rho c_p A_{\mathrm{in}} v_{\mathrm{in}} \Delta T, \tag{11}$$

$$\overline{T}_{\mathrm{wall}} = \frac{1}{A_0}\int_{A_0} T_{\mathrm{wall}}\, dA, \tag{12}$$

$$T_\infty = \frac{1}{2}(T_{\mathrm{in}} - T_{\mathrm{out}}), \tag{13}$$

where Q is the heat flux, ρ is the drilling fluid density, A_{in} is the inlet cross-sectional area, v_{in} is the inlet flow rate, ΔT is the temperature difference between the inlet and outlet, and A_0 is the total heat transfer area. T_{wall} is the average temperature of the heating wall, and T_∞ is the average temperature of the drilling fluid.

2.3. Physical model establishment

Due to the high density, elevated viscosity, and significant solid content of drilling fluid, conventional straight-tube heaters are prone to blockage. To enhance convective heat transfer performance, this study designed a spiral-finned heater. The heater consists mainly of an outer shell and a spiral-finned cylinder, with the latter serving as the core heating component.

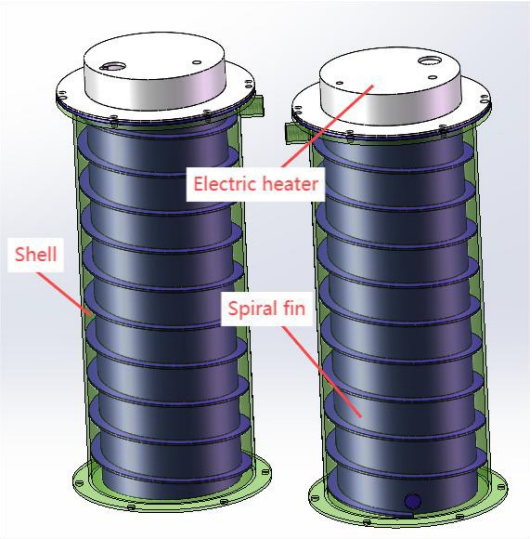

Figure 2. Spiral fin heater

Heating is achieved by using an electric heating element to raise the temperature of the inner wall of the spiral-finned cylinder. The drilling fluid enters from the bottom of the heater, flows upward against gravity, exchanges heat with the spiral-finned cylinder, and exits from the top. This counter-current flow direction increases the residence time of the drilling fluid within the heater, thereby improving heat transfer efficiency. A schematic of the spiral heater designed in this study is shown in Figure 2.

To facilitate numerical simulation, the spiral finned heater was geometrically simplified to obtain a computational model, as illustrated in Figure 3. The key structural dimensions of the heater are listed in Table 1. The geometric model was created using SolidWorks and then imported into SpaceClaim for fluid domain extraction, as well as for defining the fluid inlet and outlet, thereby laying the foundation for mesh generation.

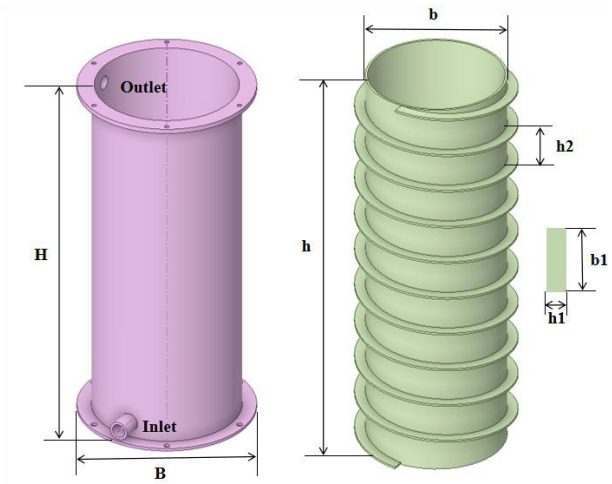

Figure 3. Simulation model of spiral heater

Table 1. Structure size of spiral heater

Structural	Parameter	Values	Structural	Parameter	Values
Enclosure	Inlet diameter D_{in}	15 mm	Spiral fin	Pitch h_2	38 mm
	Outlet diameter D_{out}	15 mm		Tooth thickness h_1	2 mm
	Inlet length L_{in}	24 mm		Tooth width b_1	10 mm
	Exit length L_{out}	24 mm		Height h	382 mm
	Shell height H	385 mm		Inner diameter b	131 mm
	Shell diameter B	187 mm		Wall thickness t	3 mm

Table 2. Parameters of drilling fluid and heater materials

Category	**Physical parameters**	**Unit**	**Value**
Drilling fluid	Density	g/cm^3	1.15
	Viscosity	mPa·s	21
	Temperature	K	300
	Thermal conductivity	$W \cdot m^{-1} \cdot °C^{-1}$	0.82
	Specific heat capacity	$J \cdot kg^{-1} \cdot K^{-1}$	4740
Steel	Density	kg/m^3	8030
	Specific heat capacity	$J \cdot kg^{-1} \cdot K^{-1}$	502.48
	Thermal conductivity	$W \cdot m^{-1} \cdot K^{-1}$	16.27

During oil and gas drilling operations, multiple factors influence the heating performance of the heater. This study focuses on the effects of spiral fin thickness, fin pitch, and heat flux density on heating performance. To ensure simulation accuracy, the thermophysical properties of the drilling fluid were based on measured data, and the heater material

was selected as steel. The relevant parameters of the drilling fluid and heater materials are provided in Table 2.

2.4. Boundary condition

Velocity inlet and pressure outlet boundary conditions were employed. The governing equations for fluid flow and heat transfer were solved using the SIMPLEC algorithm. The influence of gravity was accounted for in the simulations by specifying a gravitational acceleration of 9.8 m/s². The inner wall of the spiral finned cylinder was defined as a wall boundary with a constant and uniform heat flux. In contrast, the inner wall of the heater's outer shell was specified as adiabatic, implying that the heat generated by the heater is entirely transferred to the fluid with no losses to the environment. A steady-state simulation approach was adopted. To ensure solution convergence, the residual criteria for mass, velocity components, and energy were all set to 10^{-6}.

2.5. Mesh subdivision

In this paper, the heating characteristics of drilling fluid in the heater are studied. The spiral heater structure is meshed. In order to verify the grid independence, the spiral heater is divided into 8 kinds of grids, and the Nusselt number is counted. The simulation conditions are : viscosity is 21mPa.s, inlet velocity is 0.5m / s, heat flux is 10w / cm2. As shown in Figure 4, as the number of grid cells increases, the Nusselt number begins to decrease. The heaters were analyzed using different grid units such as 253219,381870,721443,85922,1041808,1356667,1514489 and 1932578.

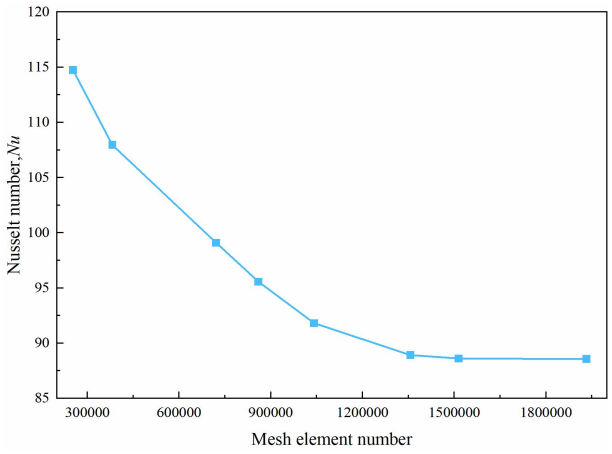

Figure 4. Grid independence verification

The Nu numbers were 114.74277,107.9532,99.09034,95.5556,91.80174,88.92485,88.60328 and 88.5102, respectively. The percentages of the last two Nu changes were 0.36% and 0.1%, respectively. The change of mesh size can obviously affect the accuracy of simulation calculation. The Nusselt number of coarse mesh is obviously higher than that of fine mesh. In order to ensure the accuracy of calculation and save the calculation time, the mesh parameter of 1356667 is selected as the computational mesh of numerical simulation.

2.6. Rheological model and justification

The drilling mud exhibits pronounced non-Newtonian characteristics, including shear-thinning behavior and a yield stress, which are critical for accurately predicting hole-cleaning efficiency and equivalent circulating density (ECD). Therefore, the Herschel–Bulkley (H–B) model was adopted to characterize its rheological behavior, as expressed in Eq. (1):

$$\tau = \tau_0 + K\gamma^n, \tag{14}$$

where τ is the shear stress, τ_0 is the yield stress, K is the consistency index, n is the flow behavior index, and γ is the shear rate.

The H–B model offers significant advantages over simpler rheological models for this application, based on the following physical considerations:

Yield Stress Capture: The presence of τ_0 allows the model to represent the gel strength of the mud at rest, which is essential for simulating barite sag and cuttings suspension during connections.

Shear-Thinning Accuracy: The power-law term $(K\gamma^n)$ more accurately captures the viscosity reduction with increasing shear rate, which dominates flow dynamics in the annulus and inside the drill pipe.

Furthermore, to account for the downhole temperature effects, the parameters of the H–B model (τ_0, K, n) were treated as functions of temperature (T). The correlations were established empirically from high-temperature, high-pressure (HTHP) rheometer measurements, as detailed in Eqs. (2)–(4).

$$\tau_0(T) = a \times \exp(-bT), \tag{15}$$

$$K(T) = c + \frac{d}{T}, \tag{16}$$

$$n(T) = e + f(T). \tag{17}$$

This temperature-dependent H-B model is therefore deemed physically comprehensive for simulating the circulating mud under downhole conditions.

3. Result and discussions

This study primarily investigates the influence of the drilling fluid Reynolds number and the structural parameters of the heater on its thermal performance. The heating performance of the spiral fin heater was evaluated based on the Nusselt number, fluid outlet temperature, and temperature distribution. For detailed analysis, five cross-sectional planes and one intermediate longitudinal section were selected, as illustrated in Figure 5.

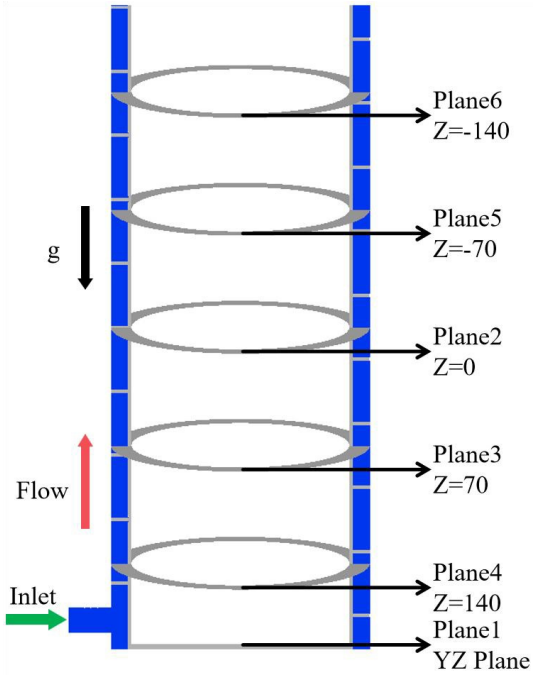

Figure 5. Schematic diagram of the selected cross plane and middle section

4. The influence of fin thickness

To analyze the influence of fin thickness and Reynolds number on the heat transfer performance, different fin thicknesses—2 mm, 4 mm, 6 mm, 8 mm, and 10 mm—were

selected for investigation. The inlet velocities of the drilling fluid were set as 0.1 m/s, 0.2 m/s, 0.3 m/s, 0.4 m/s, and 0.5 m/s, respectively, and a constant heat flux density of 10 W/cm² was applied to the inner surface of the heater.

Figure 6 illustrates the variation of the Nusselt number (Nu) with Reynolds number (Re) for different fin thicknesses. The results indicate that Nu increases with Re, though the rate of increase gradually slows. At a given Re, wider fins yield higher Nu values, and the difference in Nu between fins of different thicknesses becomes more pronounced as Re increases. At low Re, the differences are relatively small; however, they widen significantly with increasing Re. Notably, the incremental gain in Nu diminishes with increasing fin thickness: the largest difference occurs between the 2 mm and 4 mm fins, while the smallest is observed between the 8 mm and 10 mm fins.

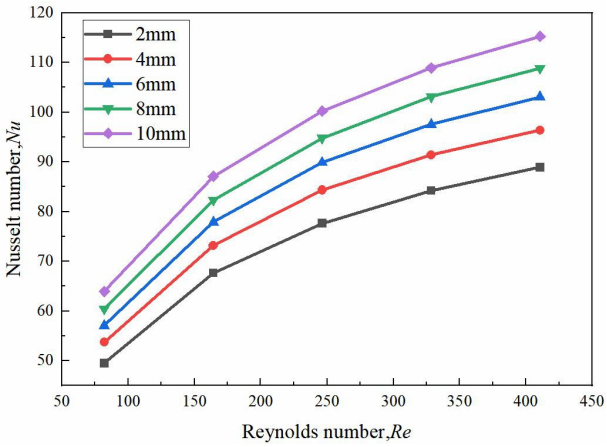

Figure 6. The Nusselt number under different fin thickness and different Reynolds number

Figure 7 shows the outlet temperature of the drilling fluid under different fin thicknesses and Reynolds numbers. The outlet temperature decreases with increasing Re, with a progressively slowing rate of decline. In general, thicker fins lead to lower outlet temperatures, and the temperature difference between different fins slightly increases at higher Re. However, the behavior of the 4 mm-thick fin is distinctive: as Re increases, its outlet temperature decreases more slowly than those of other fin thicknesses. At higher Re values, the outlet temperature for the 4 mm fin even exceeds that of the 2 mm fin, indicating superior heat transfer performance under high-flow conditions. This observation is further supported by the temperature contours at the outlet cross-section for different fin thicknesses (Figure 8), where the 4 mm fin exhibits a larger high-temperature region compared to other configurations.

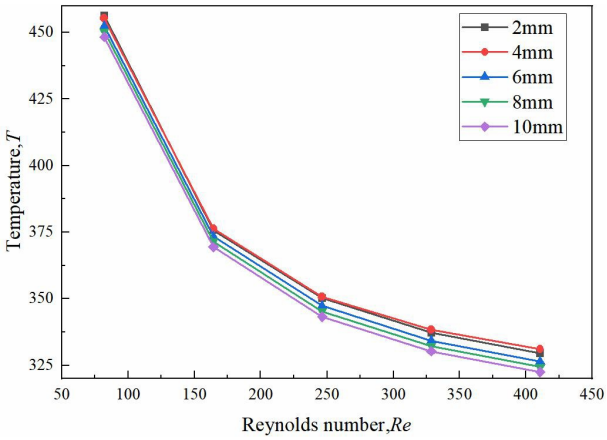

Figure 7. The outlet temperature under different fin thickness and different Reynolds number

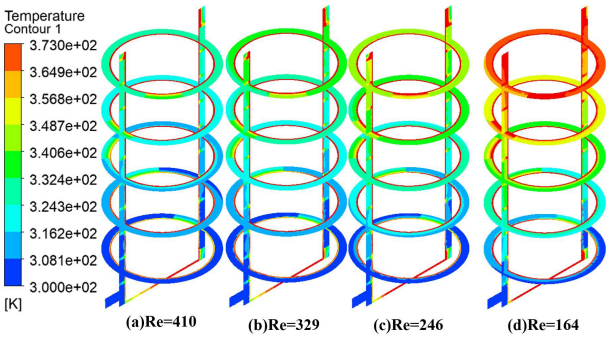

Figure 8. Temperature distribution under different Reynolds numbers with fin thickness of 4mm

Figure 9 presents the temperature distribution contours for a 4 mm fin under different Re values at a constant heat flux of 10 W/cm². Higher Re values correspond to higher fluid velocities, which shorten the residence time of the drilling fluid in the heater and thus reduce the heating effect. In contrast, lower Re values result in more pronounced heating.

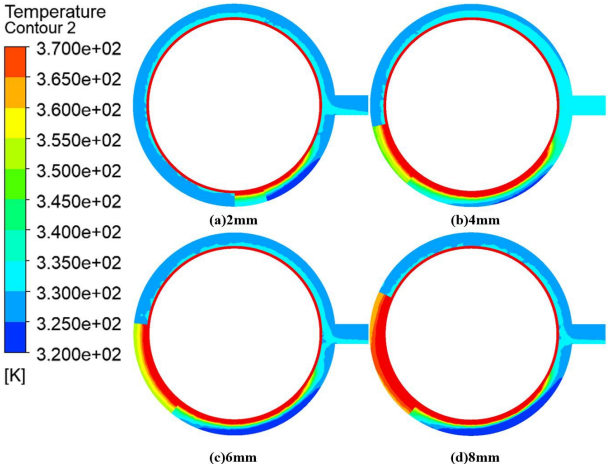

Figure 9. Temperature distribution nephogram of fin outlet section with different thickness

Figure 10 displays the velocity distribution at the inlet cross-section for different fin thicknesses (2 mm to 10 mm, top to bottom) at an inlet velocity of 0.5 m/s. The fluid velocity is highest in the central region of the inlet. The velocity gradient exhibits a multi-block pattern, resulting from the rapid radial expansion of the fluid as it enters the annular passage from the inlet pipe, with the central fluid expanding most rapidly. As the fin thickness increases, the annular flow passage narrows, leading to higher flow velocities. The velocity distribution in the annular passage takes on an elongated elliptical shape, with the central velocity rising and the velocity gradient becoming denser and more distinct as fin thickness increases.

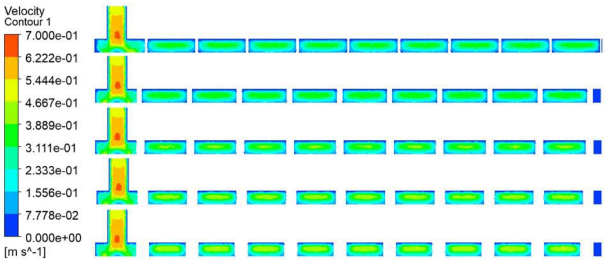

Figure 10. Velocity distribution of fins with different thicknesses at a flow rate of 0.5m/s Fig.

Figure 11 shows the pressure distribution for a 4 mm fin under different Reynolds numbers. The pressure drop decreases with decreasing Re, with values of 5529 Pa, 4183 Pa, 2935 Pa, and 1802 Pa corresponding to the tested conditions.

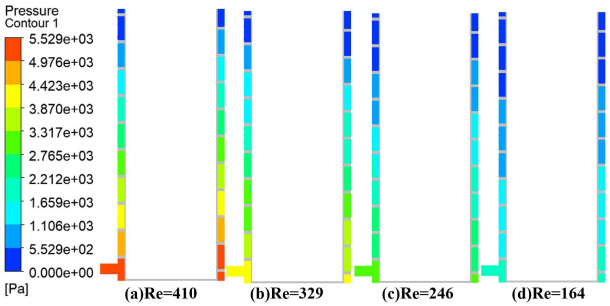

Figure 11. The pressure distribution under different Reynolds numbers with fin thickness of 4mm

4.1. The influence of fin pitch

To analyze the influence of fin pitch and Reynolds number on heat transfer performance, heaters with different fin pitches—28 mm, 38 mm, 48 mm, and 58 mm—were investigated. The inlet velocities of the drilling fluid were set as 0.1 m/s, 0.2 m/s, 0.3 m/s, 0.4 m/s, and 0.5 m/s, respectively, under a constant heat flux density of 10 W/cm² applied to the heater's inner surface.

Figure 12 illustrates the variation of the Nusselt number (Nu) with Reynolds number (Re) for different fin pitches. The results show that Nu increases with Re, though the rate of increase gradually declines. At a constant Re, Nu decreases as the fin pitch increases. The difference in Nu between different pitches becomes more pronounced at higher Re values: while the differences are relatively small at low Re, they widen significantly as Re increases. Notably, the incremental reduction in Nu diminishes with increasing pitch, with the largest difference observed between the 28 mm and 38 mm pitches, and the smallest between the 48 mm and 58 mm pitches.

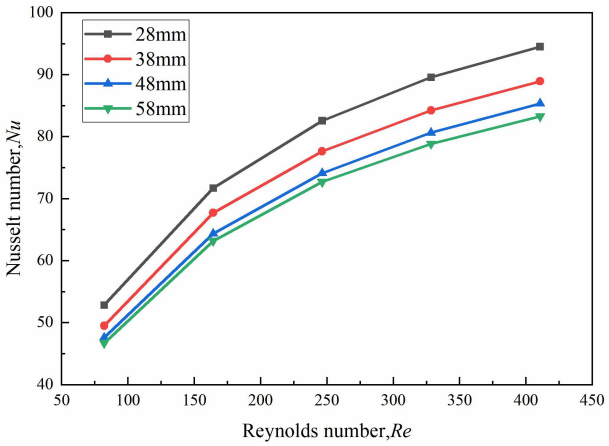

Figure 12. The Nusselt number under different pitches and different Reynolds numbers

Figure 13 presents the outlet temperature of the drilling fluid under different fin pitches and Reynolds numbers. The outlet temperature decreases with increasing Re, with the rate of decrease slowing at higher Re values. Larger fin pitches generally lead to lower outlet temperatures, and the temperature difference between different pitches increases slightly with Re. It is noteworthy that the outlet temperature for the 28 mm pitch decreases more markedly with increasing Re compared to the other pitches.

Figure 14 shows temperature distribution contours for different fin pitches at a constant Reynolds number. The heater with the 28 mm fin pitch achieves a higher fluid temperature

than those with larger pitches. This temperature advantage is particularly evident on plane 6, indicating that the 28 mm pitch provides superior heating performance.

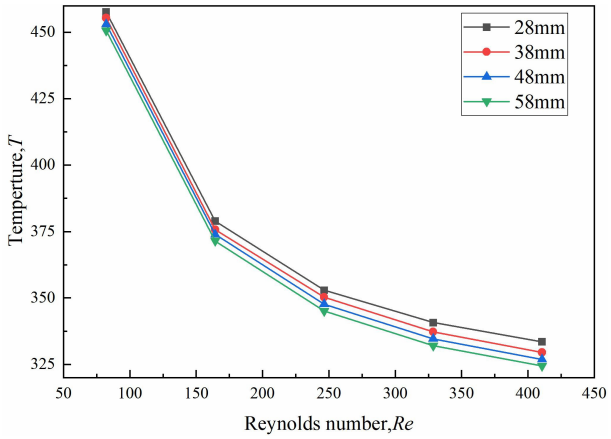

Figure 13. The outlet temperature at different pitches and different Reynolds numbers

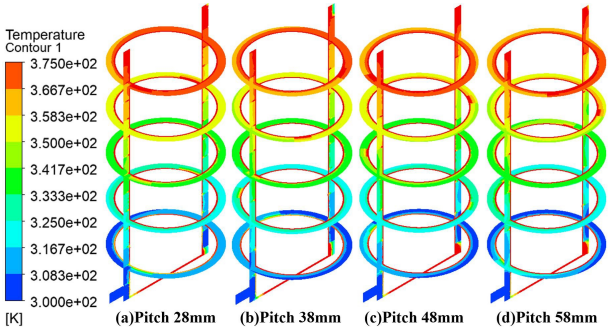

Figure 14. The temperature distribution of the middle section under different pitches

Figure 15 illustrates that the fluid undergoes considerable radial expansion upon entering the annular flow passage. Additionally, as the fin pitch increases, the flow velocity within the annular passage gradually decreases.

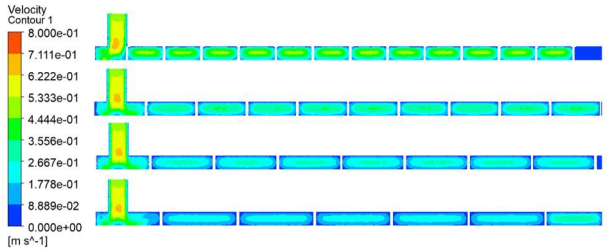

Figure 15. The velocity distribution cloud diagram of inlet section under different pitches

Figure 16 displays the pressure distribution on the mid-plane for different fin pitches at an inlet velocity of 0.5 m/s. The pressure drop decreases as the fin pitch increases, with the 28 mm pitch yielding the highest pressure drop. The measured pressure drops for pitches of 28 mm, 38 mm, 48 mm, and 58 mm are 10470 Pa, 5138 Pa, 3110 Pa, and 2371 Pa, respectively.

4.2. The influence of heat flux density

To evaluate the effect of heat flux density on heat transfer performance, numerical simulations were conducted under different heat flux conditions. The inner surface of the heater was assigned heat flux densities of 10 W/cm², 12 W/cm², 14 W/cm², 16 W/cm², 18 W/cm², and 20 W/cm², respectively.

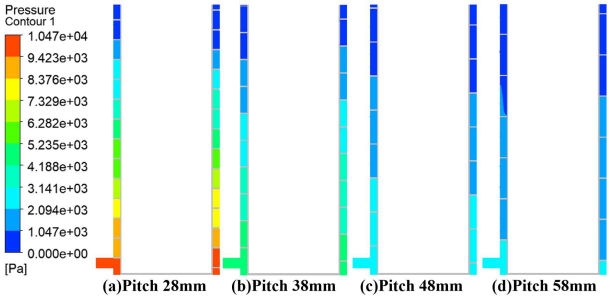

Figure 16. The pressure distribution cloud diagram of the middle section under different pitches

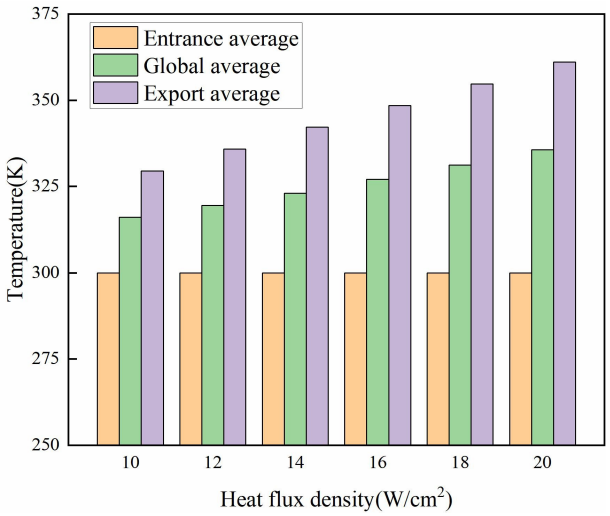

Figure 17. The inlet and outlet and the overall average temperature under different heat flux densities

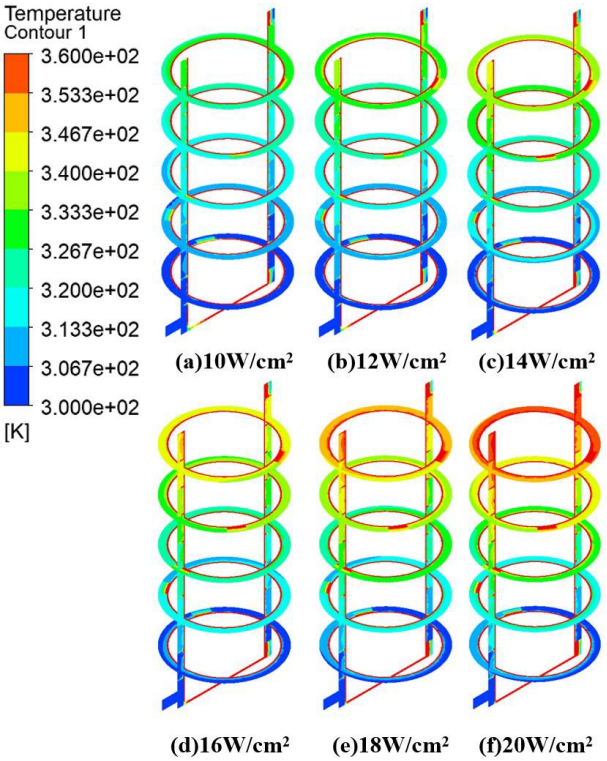

Figure 18. Temperature distribution nephogram under different heat flux density

Figure 17 compares the average inlet temperature, outlet temperature, and bulk mean fluid temperature under various heat flux densities. Both the outlet temperature and the bulk mean temperature of the drilling fluid increase nearly linearly with rising heat flux density. Figure 18 shows the corresponding temperature distribution contours for different heat flux values. As anticipated, higher heat flux densities lead to a uniform temperature rise across the entire fluid domain.

5. Experiment

5.1. Experimental method

To validate the accuracy of the numerical simulations, an experimental test bench was constructed for the spiral heater. Figure 19 shows the experimental setup, including the control and data acquisition system. A continuous heating mode was employed for the electric heater, with the wall heat flux density set to 10 W/cm² to facilitate measurement of the heater outlet temperature.

Figure 19. Experimental device of spiral heater

5.2. Experimental result

Given the practical difficulty in controlling drilling fluid viscosity during experiments, the operational parameters were designed to examine the effect of inlet velocity on outlet temperature. The drilling fluid inlet velocity was varied as 0.1 m/s, 0.2 m/s, 0.3 m/s, 0.4 m/s, and 0.5 m/s. Heaters with fin pitches of 28 mm and 38 mm were tested, and the results were compared with CFD simulation data.

As shown in Figure 20, the experimentally measured outlet temperatures are noticeably lower than those obtained from numerical simulations. This discrepancy is primarily attributed to significant thermal dissipation and other experimental errors during testing.

The largest difference between simulated and experimental temperatures, approximately 12°C, occurs at the lowest inlet flow rate of 0.1 m/s.

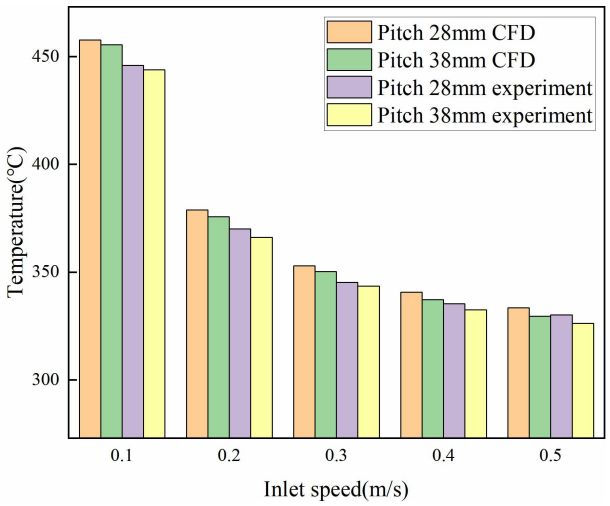

Figure 20. The difference between CFD and experimental outlet temperature

6. Conclusion

To address the challenge of heating efficiency in drilling fluid degassers, this study employed computational fluid dynamics (CFD) to investigate the flow and heat transfer characteristics of drilling fluid inside a spiral heater. The effects of key structural parameters—fin thickness and pitch—as well as operational conditions represented by the Reynolds number (Re) were systematically analyzed. The performance was evaluated based on flow field distribution, temperature profile, and Nusselt number (Nu). Experimental validation was also conducted for heaters with two different fin pitches across a range of flow rates. The main findings are summarized as follows:

1. Effect of Fin Thickness and Reynolds Number

At a constant Reynolds number, an increase in fin thickness leads to a higher Nusselt number but a lower fluid outlet temperature.

For a given fin thickness, increasing the Reynolds number enhances the Nusselt number while reducing the outlet temperature.

A distinctive behavior was observed for the 4 mm fin: the decline in outlet temperature with increasing Reynolds number was less pronounced compared to other thicknesses, indicating favorable performance under high-flow conditions.

2. Effect of Fin Pitch and Reynolds Number

At a fixed Reynolds number, reducing the fin pitch results in a higher Nusselt number and elevated outlet temperature.

For a specific fin pitch, raising the Reynolds number increases the Nusselt number but lowers the outlet temperature.

Hence, a smaller spiral fin pitch improves both the heating effectiveness and heat transfer performance of the heater.

References

[1] Fu, X., Qin, Y., Wang, G. G., & Rudolph, V. (2009). Evaluation of gas content of coalbed methane reservoirs with the aid of geophysical logging technology. *Fuel, 88*(11), 2269-2277.

[2] Wang, C., Wang, Y., Kuru, E., Chen, E., Xiao, F., Chen, Z., & Yang, D. (2021). A new low-damage drilling fluid for sandstone reservoirs with low-permeability: Formulation, evaluation, and applications. *Journal of Energy Resources Technology, 143*(5), 053004.

[3] Wang, D., Zang, R., Wang, G., Chen, J., & Peng, X. (2024). Numerical study of heat transfer performance and flow characteristic of water in a multi-wound pipe heat exchanger. *Thermal Science and Engineering Progress, 52*, 102683.

[4] Zhang, D., Zhao, L., Dong, H., & Wu, R. (2023). Experimental study on heat transfer and flow resistance characteristics of integral rolled spiral finned tube bundles heat exchangers. *Case Studies in Thermal Engineering*, *52*, 103689.

[5] Ali, N. B., Jasim, D. J., Aminian, S., Singh, P. K., Rajab, H., Elsemary, I. M., ... & Abdollahi, S. A. (2024). Numerical exploration of the impact of fluid type in a uniquely designed shell and spiral tube heat exchanger. *Case Studies in Thermal Engineering*, *61*, 104798.

[6] Kazemi-Esfe, H., Shekari, Y., & Omidvar, P. (2024). Comparison of heat transfer characteristics of a heat exchanger with straight helical tube and a heat exchanger with coiled flow reverser. *Applied Thermal Engineering*, *253*, 123772.

[7] de Vasconcelos Segundo, E. H., Mariani, V. C., & dos Santos Coelho, L. (2019). Design of heat exchangers using falcon optimization algorithm. *Applied Thermal Engineering*, *156*, 119-144.

[8] Zhang, T., Chen, L., & Wang, J. (2023). Multi-objective optimization of elliptical tube fin heat exchangers based on neural networks and genetic algorithm. *Energy*, *269*, 126729.

[9] Petrovic, M., Fukui, K., & Kominami, K. (2023). Numerical and experimental performance investigation of a heat exchanger designed using topologically optimized fins. *Applied Thermal Engineering*, *218*, 119232.

[10] Du, J., Hong, Y., Wang, S., Ye, W. B., & Huang, S. M. (2018). Experimental thermal and flow characteristics in a traverse corrugated tube fitted with regularly spaced modified wire coils. *International Journal of Thermal Sciences*, *133*, 330-340.

[11] Pérez-García, J., García, A., Herrero-Martín, R., & Solano, J. P. (2018). Experimental correlations on critical Reynolds numbers and friction factor in tubes with wire-coil inserts in laminar, transitional and low turbulent flow regimes. *Experimental Thermal and Fluid Science*, *91*, 64-79.

[12] Gunes, S., Ozceyhan, V., & Buyukalaca, O. (2010). The experimental investigation of heat transfer and pressure drop in a tube with coiled wire inserts placed separately from the tube wall. *Applied Thermal Engineering*, *30*(13), 1719-1725.

[13] Muñoz-Esparza, D., & Sanmiguel-Rojas, E. (2011). Numerical simulations of the laminar flow in pipes with wire coil inserts. *Computers & Fluids*, *44*(1), 169-177.

[14] Akyürek, E. F., Geliş, K., Şahin, B., & Manay, E. (2018). Experimental analysis for heat transfer of nanofluid with wire coil turbulators in a concentric tube heat exchanger. *Results in Physics*, *9*, 376-389.

[15] Keklikcioglu, O., & Ozceyhan, V. (2016). Experimental investigation on heat transfer enhancement of a tube with coiled-wire inserts installed with a separation from the tube wall. *International Communications in Heat and Mass Transfer*, *78*, 88-94.

[16] Promvonge, P. (2008). Thermal performance in circular tube fitted with coiled square wires. *Energy Conversion and Management*, *49*(5), 980-987.

[17] Zohir, A. E., & Habib, M. A. (2012). Heat transfer characteristics in a double-pipe heat exchanger equipped with coiled circular wires. *Journal of Engineering Sciences*, *40*(3), 731-744.

[18] Ibrahim, E. Z. (2011). Augmentation of laminar flow and heat transfer in flat tubes by means of helical screw-tape inserts. *Energy Conversion and Management*, *52*(1), 250-257.

[19] Eiamsa-Ard, S., & Promvonge, P. (2007). Heat transfer characteristics in a tube fitted with helical screw-tape with/without core-rod inserts. *International Communications in Heat and Mass Transfer*, *34*(2), 176-185.

[20] Yu, H., Sui, Y., Zhang, F., & Chang, X. A. (2005). Numerical simulation of oxygen transportation in 300 mm diameter CZ Si crystal growth under cusp magnetic field. *Bandaoti Xuebao(Chin. J. Semicond.)*, *26*(3), 517-523.